Surface crack growth in FRP repaired metallic pipes subjected to cyclic bending

19

Zongchen Li[a, b]
[a]Department of Maritime and Transport Technology, Delft University of Technology, Delft, The Netherlands; [b]Mechanical Systems Engineering, EMPA-Swiss Federal Laboratories for Materials Science and Technology, Duebendorf, Switzerland

Chapter outline

Rehabilitation of Metallic Structural Systems Using Fiber Reinforced Polymer (FRP) Composites
https://doi.org/10.1016/B978-0-443-22084-5.00008-7

19.1 Introduction

Fiber-Reinforced Polymers (FRPs) have been extensively applied for repairing damaged metallic pipes for decades, known as the Composite Repair System in the piping industry [1]. In the past decade, research has elucidated the efficacy of FRPs in repairing pipes with corrosion [2,3], holes or defects [4–7], and cracks [2,8–13]. Both FRP wrappings and patches, utilizing either Carbon-FRP (CFRP) or Glass-FRP (GFRP), have been employed to ascertain the postrepair failure pressure [7,14], Stress Intensity Factor (SIF) [2,9,10,12,13] or the J-integral [8,15] associated with the crack.

In contrast to those pipelines exposed to internal pressure, offshore metallic pipes, including risers, are subjected to sustained dynamic forces due to oceanic waves, winds, currents, and second-order floater motions [16]. Notably, these pipelines maintain a near-equilibrium between internal and external pressures. These dynamic forces result in significant cyclic axial stresses, manifesting as tension and/or bending on the pipeline. Consequently, this can induce the initiation and propagation of surface cracks, culminating in potential leakages or fractures.

The finite element method (FEM) has been extensively applied to the investigations of composite reinforcement on cracked metallic structures over the past decades. The FEM assists users to better understand the mechanism by analyzing the structural mechanical behavior (e.g., deformation, stress concentration), fatigue indicator parameters such as SIF and J-integral [17–20], and bond failures [21,22]. New methods such as extended-FEM [23], S-version FEM [24], and the iso-geometric analysis method [25,26] have been developed as efficient alternatives for handling fatigue crack growth analysis. In recent years, the effect of bond failures on crack growth when employing composite reinforcement has received increasingly attention [27]. Cohesive zone modeling (CZM) has been incorporated into the finite element (FE) model to analyze the bond condition and its influence on the crack growth [21,22,28].

A reliable analytical approach owns considerable value by virtue of its user-friendly feature, high efficiency, and rational accuracy. In addition, neat formulas within an analytical approach enable users to intentionally comprehend its mechanism and to quantify each parameter. Previous studies that focused on analytical approaches have made good attempts to predict crack growth in metallic components reinforced with FRP. Wang and Rose [29] proposed a crack bridging model to calculate the SIF of central cracks in plates with a one-side bonded patch. Liu et al. [30] conducted a theoretical study of the central-crack growth in CFRP repaired steel plates through the analysis of the strain distribution in the FRP layers and the stress distribution at the cracked section. Semianalytical methods by combing finite element analysis (FEA) to determine correction factors for the analytical approach were proposed in the past decade as well. Yu et al. [31] used linear-elastic fracture mechanics (LEFM) to evaluate the SIF at crack tips of CFRP bonded steel plates, where FEA was adopted to calculate the geometry correction factor, so did the study by Wang et al. [32] on the SIF of double-edged cracks.

We were aware of the fact that the effectiveness of FRP reinforcement in reducing crack growth rate owes to the decreasing stress field and the crack-bridging effect

when FRP laminates contact the cracked surface [33,34]. The crack-bridging effect on decreasing crack growth rate may not be simply presented as a constant value. With further comprehension of adhesive bonding mechanism, researchers realized the importance of interfacial bond behavior [21,22]—debonding failure could reduce the reinforcement efficiency. This is in general known as the crack-induced debonding [22] or stiffness degradation [33] in the scenario of using FRP to repair cracked structures, usually considered via the CZM [35−37]. The traction-separation law, on which the CZM is based, is adequate for reinforced structures under static or monotonic loads. However, it is insufficient for cases under cyclic loads since the bond interface could suffer from fatigue damage simultaneously [38]. Therefore, when analyzing crack growth in metallic structures reinforced with FRP under cyclic loads, interfacial fatigue damage shall be integrated into the traction-separation law. Hence, a real-time crack-bridging effect on crack growth can be rationally considered.

The utilization of FRP for repairing surface cracks in metallic pipes presents unique challenges, distinguishing it from the repair of through-thickness cracks typically encountered in other scenarios [16]. Furthermore, the cylindrical geometry and specific load conditions of pipes introduce further distinctions compared to cracks in flat plates. Given those concerns, this study conduct an in-depth investigation though experimental, FEA, and analytical approaches, to comprehensively assess the FRP repair on surface crack pipes, and to understand the mechanism of the repairing on decreasing the crack propagation. The experimental, FEA, and the analytical approach are presented in Sections 19.2−19.4, respectively. All results are integrated and discussed in Section 19.5. Finally the conclusions are drawn in Section 19.6.

19.2 Experimental investigation

19.2.1 Specimen preparation

Material properties

Reinforced external surface cracked steel pipe specimen is illustrated in Fig. 19.1. Four materials were used to manufacture the specimens: steel substrate, GFRP, CFRP, and adhesive. Stainless steel *API 5L X65* for subsea scenarios conforming to API SPEC 5L code [39] has been used as the steel substrate. In light of the galvanic corrosion between the CFRP laminates and the steel substrate, one layer of GFRP laminate was adopted as the contact inhibitor between the steel substrate and CFRP laminates. The detailed material properties are listed in Tables 19.1−19.4. Note that all material properties are provided by their supplies.

Specimen manufacturing

The specimen manufacturing contains three main steps: manufacturing notches, precracking, and the FRP reinforcement. Semi-elliptical notches located in the mid-bottom of the steel pipes were manufactured. They were made by the ASTM E2899 suggested Micro-Electric Discharging Machining (Micro-EDM) method in order to

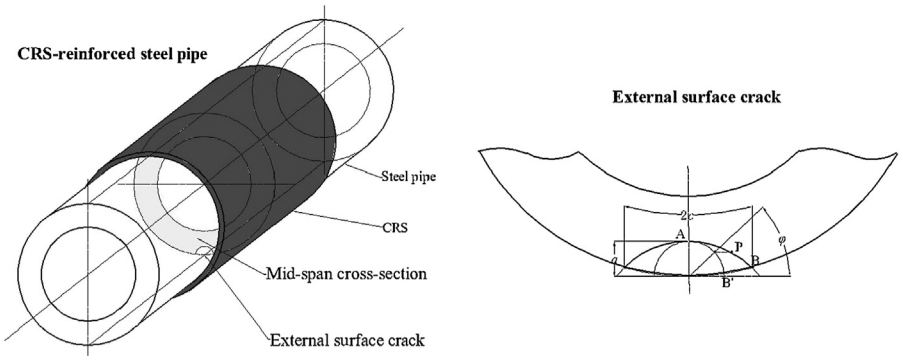

19.1 The sketch diagram of the FRP reinforced surface cracked pipe specimens.

achieve the user designed notch profile and to avoid the thermal residual stress [41]. The width and half-length of all notches are controlled as 0.35 and 4.0 mm respectively. The shape of the notches guaranteed that the surface cracks would propagate as semi-elliptical shaped during the fatigue tests.

Then, a pre-cracking procedure was conducted on the notched steel pipes, in order to initiate fatigue cracks from the notches [42]. This procedure was conducted on the fatigue machine using the four-point bending, containing two stages: the first stage adopted 80% yield stress of the steel as the amplitude of the sinusoidal cyclic loading, while the second stage adopted 60% yield stress. Note both stages were conducted under the load ratio R equals to 0.1. The pre-cracking procedure continued until the surface crack initiated from the notch and propagated more than 1.0 mm along the length direction, which was monitored by an electronic microscope. Then the size of each surface crack after the pre-cracking procedure was regarded as the initial crack size.

Afterward, the external surface cracked steel pipes were reinforced with FRP, containing three procedures: surface preparation, cleaning, and pasting the composite laminates onto the steel substrate. The rust cleaning and sanding process were implemented during the surface preparation procedure. Then the surface of the steel substrate was cleaned using acetone. After wrapping multiple layers following the reinforcement schemes, the FRP were compressed by wrapping plastic tapes around the external composite layer to squeeze redundant resin epoxy and eliminate the bubbles in the interlaminations. This process guaranteed that the FRP was bonded tightly onto the steel pipe. Finally the reinforced specimens were placed at room temperature for solidification of 1 week, in order to achieve the optimum bond condition.

Specimens configurations

The dimensions of the selected specimens are listed in Table 19.5, including the pipe length L, pipe external diameter D, wall thickness of the pipe specimens t, and the depth & half length of the notch a_0 and c_0. The thickness of each layer of GFRP and CFRP laminate are 0.35 mm. The thickness of the adhesive between the steel and the GFRP is 0.2 mm. In total, nine groups of 27 specimens were prepared. Group

Table 19.1 Material properties of *API 5L X65* steel

***E* (Pa)**	***Y* (Pa)**	***T* (Pa)**	***v***
206×10^9	4.48×10^9	5.3×10^9	0.3

E, is the tensile elastic modulus; *T,* is the tensile strength; *v,* is the Poisson's ratio; *Y,* is the yield strength.

Table 19.2 Material properties of the GFRP

E_1 (Pa)	E_2 (Pa)	E_3 (Pa)	G_{12} (Pa)	G_{13} (Pa)	G_{23} (Pa)	v_{12}	v_{13}	v_{23}
72×10^9	72×10^9	8×10^9	4.7×10^9	4.7×10^9	3.5×10^9	0.28	0.28	0.08

E_i and G_{ij} are the elastic modulus and shear modulus along different directions, v_{ij} is the Poisson's ratio of the *i-j* plane.

Table 19.3 Material properties of the CFRP (Toray T700S series)

E_1 (Pa)	E_2 (Pa)	E_3 (Pa)	G_{12} (Pa)	G_{13} (Pa)	G_{23} (Pa)	v_{12}	v_{13}	v_{23}
230×10^9	25×10^9	25×10^9	5.5×10^9	5.5×10^9	3.9×10^9	0.33	0.33	0.054

Table 19.4 Material properties of the resin epoxy (Faserverbundwerkstoffe L20 resin epoxy with hardener EPH 161 [40])

***E* (Pa)**	***T* (Pa)**	***G* (Pa)**	***Nu***
2.80×10^9	70×10^6	1.4×10^9	0.35

Table 19.5 Specimens' configuration and reinforcement details

Group	Specimen	L (mm)	D (mm)	t (mm)	a_0 (mm)	c_0 (mm)	L_c (mm)	CFRP wrapping scheme
1	PE-1(1)	2000	168.3	12.76	2.31	4.94	–	–
	PE-1(2)	2000	168.3	12.81	2.48	5.04	–	–
	PE-1(3)	2000	168.3	12.77	2.44	4.89	–	–
R1	PE-1-R(1)	2000	168.3	12.63	2.31	4.94	1000	L-L-L-H
	PE-1-R(2)	2000	168.3	12.78	2.48	5.035	1000	L-L-L-H
	PE-1-R(3)	2000	168.3	12.76	2.44	4.885	1000	L-L-L-H
R8	PE-1-R8(1)	2000	168.3	12.77	2.56	5.09	1000	L-L-L-H-L-L-L-H
	PE-1-R8(2)	2000	168.3	12.72	2.56	4.90	1000	L-L-L-H-L-L-L-H
	PE-1-R8(3)	2000	168.3	12.63	2.48	5.15	1000	L-L-L-H-L-L-L-H
R45	PE-1-R45(1)	2000	168.3	12.74	2.46	4.95	1000	Inversely diagonal
	PE-1-R45(2)	2000	168.3	12.70	2.50	4.875	1000	Inversely diagonal
	PE-1-R45(3)	2000	168.3	12.79	2.52	4.87	1000	Inversely diagonal

The parameters, i.e., D, t, a_0, c_0 were measured based on each specimens, each of which is the weighted average of three measurement locations. The three notch categories represent the three different notch sizes shown in Fig. 19.2, i.e., aimed aspect ratio of 0.5, 0.625, and 1.0.

1 is the controlling group without composite reinforcement. Groups R1 used different reinforcement scheme: G1 applies four layers of CFRP laminates, the "L-L-L-H" wrapping pattern (L represents longitudinal wrapping pattern, while H represents hoop wrapping pattern) shown in Fig. 19.2a, and 1000 mm bond length. The specimens in Groups R8 applied the same wrapping pattern of Group R1, while using eight layers of CFRP instead of four layers. Group R employed an inversely diagonal

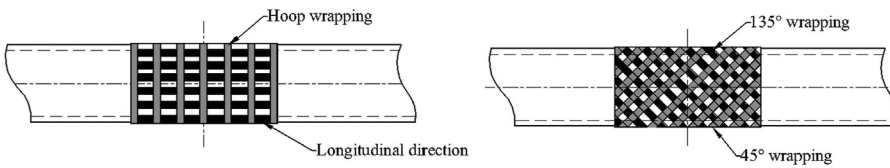

19.2 Wrapping scheme: (a) The longitudinal and hoop wrapping pattern; (b) the inversely diagonal wrapping pattern.

wrapping method, as indicated in Fig. 19.2b. Table 19.5 summarized the configuration and reinforcement details of all specimens. The name of the specimens represents the notch category, FRP reinforcement scheme, CFRP wrapping pattern, and their repetitive number. Take "PE-1-R(1)" as an example, "P" means steel pipe, "E" represents external surface crack, the "1" stands for the notch category 1, R means reinforcement, and the "(1)" means the No. of the repetitive specimen.

19.2.2 Test set-up

The fatigue tests followed the code of ASTM E647 [42]. All tests were carried out under constant amplitude sinusoidal cyclic loading, generated by MTS Hydraulic Actuator, which has a capacity of 1000 kN. The test set-up is shown in Fig. 19.3. The load was applied in four-point bending condition to ensure a pure bending statue around the cracked location within the inner span. Note that the inner span L_i is designed as 800 mm, which is more than four times larger than the pipe diameter, in order to eliminate potential negative effects from the loading cells. The external span L_e is designed as 1800 mm, therefore leaving the bending arm equals to 500 mm.

All the fatigue tests were conducted at room temperature and air environment under load control condition. The amplitude of the applied force, namely 241.54 kN, produced a maximum stress value of 268.8 MPa, accounting for 60% of the yield strength of the steel substrate. Such selection is based on the fact the normal stress at the critical zones of a steel lazy-wave riser can reach 240 MPa or even higher [43], as well as considering to adequately reducing the test period. The loading frequency was set as 2.5 Hz. The load ratio R maintained 0.1 for the crack growth process of all tests. The crack growth process was recorded using beach marking technique by means of changing the load ratio R to 0.5 and cycled for 5000 cycles. Each test ended automatically once the pipe specimen fractured.

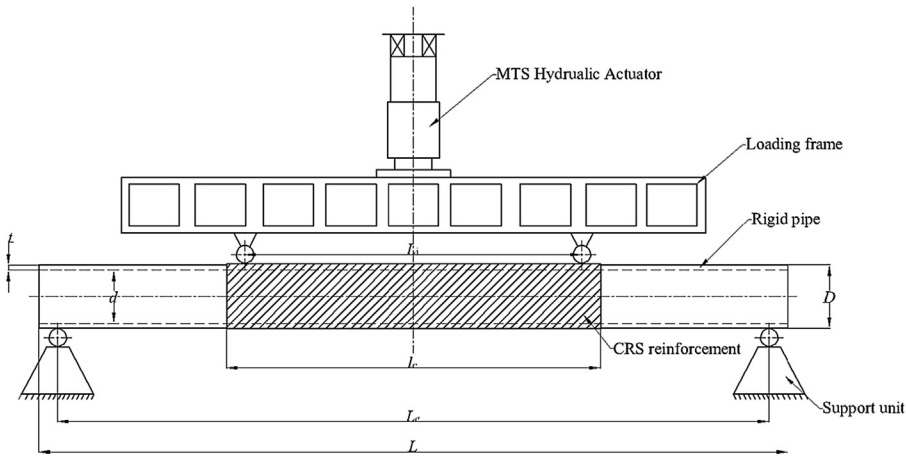

19.3 The schematic of the four-point bending test set-up.

19.3 Numerical investigation

In this section, the FE models of surface cracked metallic pipes reinforced with FRP are developed. SIF distributed along the crack front has been calculated. FRP-to-steel interfacial bond condition is analyzed by means of the CZM, and its effect on the SIFs along the crack front is taken into consideration.

19.3.1 Interfacial properties

The FE model is identical to the geometry of the test specimens indicated in Fig. 19.1, as well as the material properties of each components. In addition, a CZM technique has been dedicated to the FRP-to-steel interface, adopting a mixed-mode traction separation model, as indicated in Fig. 19.4 which interfacial properties are listed in Table 19.6.

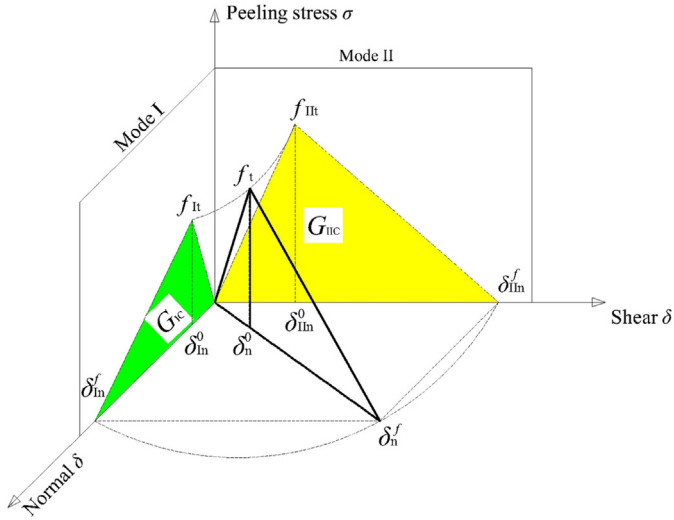

19.4 The mixed-mode traction-separation law.

Table 19.6 Mixed-mode traction-separation model properties at the FRP-to-steel interface

Mode type	f_t (MPa)	δ_n^0 (mm)	δ_n^f (mm)	K (MPa/mm)	G_c (N/mm)	ε_f
Mode-I (tension)	70.20	0.004	0.019	17,000	0.667	0.095
Mode-II (shear, tangential)	56.16	0.011	0.16	5095	4.488	

For the Mode-I case, the separation displacement δ_n^0 when the traction stress reaches the maximum f_{It}, is

$$\delta_{\mathrm{In}}^0 = \frac{t_a \cdot f_{\mathrm{It}}}{E} \tag{19.1}$$

where t_a is the thickness of the adhesive.

The energy release rate is the triangle area surrounded by the curve and the coordinate axis, which is

$$G_{\mathrm{IC}} = \frac{1}{2} f_{\mathrm{It}} \cdot \delta_{\mathrm{In}}^f \tag{19.2}$$

where δ_{In}^f is the separation displacement when debonding/delamination occurs, which is

$$\delta_{\mathrm{In}}^f = \varepsilon_f \cdot t_a \tag{19.3}$$

where ε_f is the elongation ratio.

The slope of the ascending part equals to the shear stiffness of the adhesive layer, which is

$$k = \frac{f_{\mathrm{It}}}{\delta_{\mathrm{In}}^0}. \tag{19.4}$$

For the Mode-II case, the variables of the traction-separation law is calculated using the method given by Ref. [44]. G_{IIC} is calculated as

$$G_{\mathrm{IICs}} = G_{\mathrm{IICt}} = 31 \cdot \left(\frac{f_{\mathrm{IIt}}}{G}\right)^{0.56} \cdot {t_a}^{0.27}. \tag{19.5}$$

where G is the shear modulus of the adhesive. The traction force is estimated as

$$f_{\mathrm{IIt}} = 0.8 \cdot T, \tag{19.6}$$

and δ_{IIn}^0 is calculated as

$$\delta_{\mathrm{IIn}}^0 = \frac{t_a \cdot f_{\mathrm{IIt}}}{G}, \tag{19.7}$$

δ_{IIn}^f is calculated as

$$\delta_{\mathrm{IIn}}^f = \frac{2G_{\mathrm{IIC}}}{f_{\mathrm{IIt}}}, \tag{19.8}$$

The interfacial properties calculated by Eqs. (19.1)−(19.8) are listed in Table 19.4. The degree of the interfacial stiffness degradation is represented by the scalar stiffness degradation variable (SDEG) from 0 to 1. Fully debonding occurs when meeting the condition indicated in Eq. (19.9), where the SDEG value evaluated by the FE model exceeds 1.0.

$$\left(\frac{G_{\mathrm{I}}}{G_{\mathrm{IC}}}\right)^2+\left(\frac{G_{\mathrm{IIs}}}{G_{\mathrm{IICs}}}\right)^2+\left(\frac{G_{\mathrm{IIt}}}{G_{\mathrm{IICt}}}\right)^2=1, \tag{19.9}$$

where G_{IICs} and G_{IICt} stand for the Mode-II energy release rate in two shear directions.

19.3.2 Modeling strategy

The FE modeling and analysis are conducted in ABAQUS CAE [45]. Figure 19.5a illustrates the three-dimensional model and its meshing condition. The size of the model conforms to the test specimens in the previous experimental study. A quarter surface crack as a semi-elliptical shape is modeled at the mid-bottom of the pipe, locating at the X−Y plane, as shown in Fig. 19.5b and c.

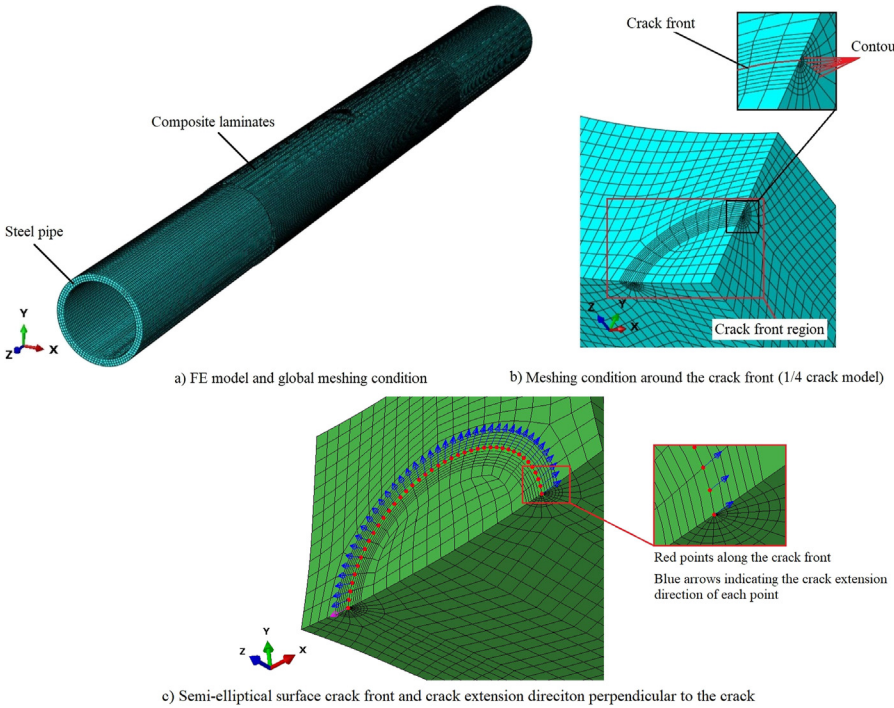

19.5 The FE model and the meshing condition: (a) the whole model and global meshing; (b) model and meshing around the crack; (c) crack front and the set-up of crack extension direction.

The FE models are developed based on the physical situation that the overall patch thickness (including adhesive layer and the composite laminates). All composite laminates are modeled as a whole. The different layers of composite laminates were merged together while remaining their own material properties and fiber directions. While each laminate remains its own material properties and orientation. One layer of adhesive is modeled between the CFRP laminates and the steel substrate through the CZM. The steel pipe excludes the crack front region, and the composite laminates, apply the 20-node quadratic brick element C3D20, while the crack front area adopts the 15-node quadratic triangular prism element C3D15. The reason of adopting quadratic brick element, including the C3D20 and C3D15 element is they are excellent for three-dimensional linear elastic calculations. The C3D15 element is applied to meet the requirement of the wedge element shape at the crack front when using contour integral method. The standardized 8-node three-dimensional cohesive element COH3D8 is used in the adhesive layer, to simulate the interfacial bond condition between the steel substrate and the composite laminate. Different meshing methods are adopted to ensure a robust and accurate evaluation. The FE model excluded the crack front region and the adhesive layer adopt the hexahedron element by the structural meshing method. While the crack front region and the adhesive layer applies the sweep meshing methods, using wedge element and hexahedron element, respectively. Under the premise of accurate evaluation, different element sizes are assigned in different areas of the FE model to reduce the computational time. The size of the wedged elements in the crack front region is controlled by the six concentric contours and 24 divisions on each of those, as indicated in Fig. 19.5b. The diameter of the external contour is 1.0 mm, and the crack front has been divided into 22 pieces. The mesh size of the area in the steel pipe adjacent to the crack front area, as well as the adhesive layer and the composite laminates are set as 1.0 mm, while the size of the pipe away from the crack front area is set as 5.0 mm. Eventually, the same bending moment of the experimental approach is applied on the pipe to calculate the SIF along the crack front, via the contour integral method. Then the relation between the crack size and the cyclic numbers is evaluated by the Paris' law. The Paris' constants are $C_A = 1.894 \times 10^{-15}$ and $m_A = 3.664$ for crack growth along the depth direction, and $C_B = 8.462 \times 10^{-16}$ and $m_B = 3.785$ for along the length direction, with the SIF unit of MPa/mm$^{0.5}$, obtained from the experimental study [16].

19.4 Analytical approach

The analytical approach is proposed in this section, highlighting key aspects such as stress degradation adjacent to cracks, the crack-bridging effect, stiffness degradation, and fatigue damage at the FRP-to-metal interface. In essence, the FRP reinforcement alters the boundary conditions of the surface crack's propagation within pipes by modifying the stress distribution and introducing the crack-bridging effect.

19.4.1 Methodology

Stress reduction

When subjected to a bending moment, each layer, resembling a hollow cylinder, experiences the same curvature. Consequently, by evaluating the overall curvature, considering the total applied bending moment and the equivalent stiffness of the entire reinforced structure, the bending moment borne by the metallic pipe can be determined. Subsequently, the normal stress within the pipe adjacent to a surface crack can be computed.

Crack-bridging effect on the surface point of a crack

In the context of circumferential surface cracks in a metallic pipe, they typically exhibit a semi-elliptical shape characterized by the crack faces and the semi-elliptical crack front. As shown in Fig. 19.6. The most crucial points along the crack front are the surface points (B_1 and B_2) and the deepest point (A), as they play a significant role in determining the crack profile, propagation rate, and path. The crack-bridging effect specifically impacts the growth of the surface crack in the longitudinal direction (X-axis). It functions as a series of distributed springs connecting the crack faces at both ends, thereby imposing a closure force on the crack tip opening displacement (CTOD) at the surface points.

It is important to note that this study primarily focuses on the crack-bridging effect at the surface points of the surface crack, where the CTOD represents the crack opening value infinitesimally close to these points. Consequently, the CTOD is equivalent to the separation at the FRP-to-metal interface. In the case of LEFM, the CTOD and SIF at the surface point can be interrelated. By incorporating the traction stress at the surface point into an equation, the SIF at that location can be determined. However, it should be emphasized that the traction stress at the deepest point is not considered since the FRP laminates do not make contact with it. Furthermore, it is important to acknowledge that the traction stress is not constant, as it is governed by interfacial properties and influenced by fatigue damage within the interface.

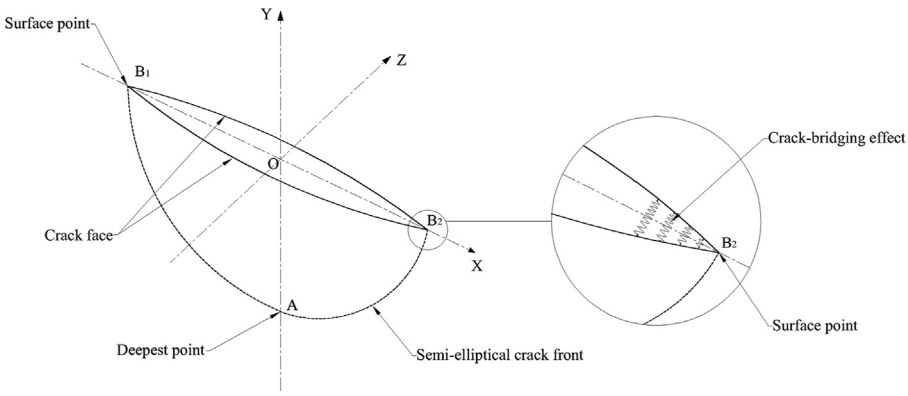

19.6 A semi-elliptical surface crack and crack-bridging effect on the crack tip at the surface point.

- FRP-to-metal interfacial bond condition

A CZM is applied to consider the FRP-to-metal interfacial bond condition. When a pipe is subjected to a bending moment, the FRP-to-metal interfacial traction stress is predominated; therefore, a bilinear traction-separation law is employed, as shown in Fig. 19.4. Different from the FEA, only one mode is considered in the analytical approach. Therefore, the $\delta_{\mathrm{IIn}}^{0}$, $\delta_{\mathrm{IIn}}^{f}$, f_{IIt} are replaced by δ_0, δ, and σ_0, respectively. At the first stage along the bilinear curve, the traction stress σ_c increases with the rising of the separation, while σ_c reaches the maximum value of σ_0 when the separation gets to δ_0. After that, the traction stress decreases gradually along the further increase of the separation value, known as stiffness degradation. Eventually, the traction stress completely disappears when the separation reaches the maximum δ, indicating the occurrence of debonding failure when the crack-bridging effect completely loses its effectiveness on the crack opening at the surface point.

- Fatigue damage of the FRP-to-metal interface under cyclic loads

In the case of implementing FRP reinforcement under cyclic loads, fatigue damage in the FRP-to-metal interface shall be considered. In this section, the FRP-to-metal interfacial fatigue damage is represented by the decreasing of traction stress, which is a function of cyclic numbers, governed by the bilinear traction separation law [38]. To better understand, initially the maximum traction stress is σ_0, while it will decrease to $\sigma_{0,i}$ when the cyclic number N reaches i. Eventually, the maximum traction stress reaches zero after a certain number of cycles, indicating a complete fatigue failure at the FRP-to-metal interface.

The methodologies described above provide a solution for determining the applied stress field and the crack-bridging effect at the surface point. To calculate the SIF at the surface point, the two near-field stresses can be superimposed and integrated into the analytical approach proposed in our previous publication [16]. This approach allows for an accurate estimation of the SIF, taking into account the combined effects of the stress field and the crack-bridging effect.

19.4.2 The analytical approach to calculate SIFs

This subsection presents the deduced and proposed analytical approach. The first step involves calculating the stress distribution in an FRP-reinforced pipe subjected to bending. Subsequently, we present the approach specifically designed for external surface cracks.

Stress distributed in a pipe reinforced with FRP subjected to bending moment

When an FRP reinforced pipe is subjected to bending, the total bending moment $M_{\mathrm{b,total}}$ equals to the sum of bending moment shared by each layer $M_{\mathrm{b},i}$, as

$$M_{\mathrm{b,total}} = \sum M_{\mathrm{b},i}, \tag{19.10}$$

$$M_{\mathrm{b},i} = C \cdot E_i \cdot I_i. \tag{19.11}$$

where C is the curvature of all layers. The $E_i \cdot I_i$ is the bending stiffness, where E_i is the elastic modulus of the layer i. I_i is the second moment of area, which is

$$I_i = \frac{\pi}{4} \cdot \left(R_i^4 - r_i^4\right). \tag{19.12}$$

where R_i and r_i are the external and internal radius of the layer i. Therefore, C is calculated as:

$$C = \frac{M_{\text{b,total}}}{\sum E_i \cdot I_i}. \tag{19.13}$$

Since all layers share the same curvature, the maximum bending moment shared by one individual layer can be calculated by Eq. (19.10). Then the normal bending stress of the steel pipe at the external surface along the longitudinal direction, $\sigma_{\text{p,b,max}}$, can be calculated as:

$$\sigma_{\text{p,b,max}} = M_{\text{b,p}} \Big/ \left[\frac{\pi \cdot R_{\text{p}}^3}{4} \cdot \left(1 - \frac{r_{\text{p}}^4}{R_{\text{p}}^4}\right)\right], \tag{19.14}$$

$$\sigma_{\text{p,b}} = G \cdot \sigma_{\text{p,b,max}}, \tag{19.15}$$

where $\sigma_{\text{p,b,max}}$ is the maximum stress when a pipe is subjected to bending, $M_{\text{b,p}}$ is the bending moment shared by the metallic pipe, R_{p}, r_{p} are the external and internal radius of the metallic pipe, $\sigma_{\text{p,b}}$ is the stress adjacent to a certain point along the surface crack front, G is the geometry correction factor when the pipe is subjected to bending [16]. For external surface cracks,

$$G = \frac{D_{\text{p}} - 2a \cdot \sin\varphi}{D_{\text{p}}}, \tag{19.16}$$

where φ is the eccentric angle of a surface crack. The eccentric angle of the deepest point equals to $\pi/2$, while the eccentric angle of the surface point φ_c is calculate as

$$\varphi_c = \frac{\pi}{2} - \frac{\pi - \frac{c}{\frac{D_{\text{p}}}{2}}}{2} = \frac{c}{D_{\text{p}}}, \tag{19.17}$$

where c is the half crack length of a surface crack. In case the FRP reinforced pipe is subjected to tension and bending simultaneously, the overall normal stress distribute is calculated by Eq. (19.9) since they could be linearly superposed as

$$\sigma_{\text{p}} = \sigma_{\text{p,t}} + G \cdot \sigma_{\text{p,b,max}}. \tag{19.18}$$

SIF calculation

Stress decreased by the crack-bridging effect needs to be considered when reinforcing external surface cracks. Hence, σ_p in Eq. (19.17) shall be amended as $\sigma_{p,c}$, which is

$$\sigma_{p,c} = \sigma_p - \sigma_c. \tag{19.19}$$

σ_c is the traction stress at the surface point owing to the crack-bridging effect. Thus the SIF at the surface point of the crack, K_{IB}, is

$$K_{I,B} = \sigma_{p,c} \cdot \sqrt{\pi \frac{a}{Q}} \cdot F. \tag{19.20}$$

In addition, stiffness degradation at the composite-to-steel interface has to be considered. The σ_c can be regard as the traction stress is determined using the traction-separation law (see in Fig. 19.4),

$$\sigma_c = \begin{cases} k_1 \cdot \delta_c & (\delta_c \le \delta_0) \\ k_2 \cdot \delta_c + b_2 & (\delta_0 < \delta_c < \delta), \\ 0 & (\delta_c \ge \delta) \end{cases} \tag{19.21}$$

where k_1 and k_2 can be obtained as

$$k_1 = \frac{\sigma_0}{\delta_0}. \tag{19.22}$$

$$k_2 = \frac{-\sigma_0}{\delta - \delta_0}. \tag{19.23}$$

$$b_2 = \frac{\sigma_0 \cdot \delta}{\delta - \delta_0}. \tag{19.24}$$

where δ and δ_0 are interfacial properties given by the traction-separation law.

In addition, the fatigue damage of the FRP-to-metal interface is considered in the traction-separation model to calculate the real-time maximum traction stress, as shown in Fig. 19.4. The decreasing rate of the maximum traction stress σ_0 is calculated as,

$$\frac{\Delta\sigma_0}{\Delta N} = \begin{cases} \alpha(\varepsilon_s - \varepsilon_{th})^{\beta}, \varepsilon_{max} > \varepsilon_{th} \\ 0, \qquad\qquad \varepsilon_{max} \le \varepsilon_{th} \end{cases}, \tag{19.25}$$

where $\Delta\sigma_0$ is the increment of fatigue damage, ΔN is the cycle increment. ε_{th} is the threshold strain meaning that the interfacial fatigue damage only occurs when ε_s is

larger than ε_{th}. α and β are material constants. ε_s is the maximum principal strain in the cohesive element, as:

$$\varepsilon_s = \frac{\delta_c}{t_a}, \tag{19.26}$$

where t_a is the thickness of the adhesive layer at the FRP-to-metal interface. Since the local displacement at the crack tip is defined as the CTOD, which can be inter-converted with the SIF under the plane stress condition [46], therefore

$$\delta_c = \mathrm{CTOD} = \frac{4K_{IB}^2}{\pi \cdot E_p \cdot \sigma_y}, \tag{19.27}$$

where E_p is the elastic modulus of a metal pipe.

Therefore, combing Eqs. (19.18)−(19.20), K_{IB} can be calculated as independent variable in a quadratic equation as one variable, as:

$$K_{I,B} = \begin{cases} \left(\sigma_p - k_1 \cdot \delta_c\right) \cdot \sqrt{\pi \dfrac{a}{Q}} \cdot F & (\delta_c \le \delta_0) \\ \left[\sigma_p - k_2 \cdot \delta_c - b_2\right] \cdot \sqrt{\pi \dfrac{a}{Q}} \cdot F & (\delta_0 < \delta_c < \delta). \\ \sigma_p \cdot \sqrt{\pi \dfrac{a}{Q}} \cdot F & (\delta_c \ge \delta) \end{cases} \tag{19.28}$$

Since the bridging effect does not affect the SIF at the deepest point of the surface crack,

$$K_{I,A} = \sigma_p \cdot \sqrt{\pi \frac{a}{Q}} \cdot F. \tag{19.29}$$

Then the SIF at the surface point and the at deepest point can be calculated via the analytical method in Ref. [16], with the redefined σ_p.

To calculate the SIF based on the proposed analytical approach, a bilinear traction-separation law has been assigned in the FRP-to-steel interface, with the maximum traction stress $\sigma_0 = 56.16$ MPa when the separation δ_0 reaches 0.011 mm. The maximum separation is $\delta = 0.16$ mm. In addition, the fatigue damage parameters of the adhesive are $\alpha = 1.5$, $\beta = 2$, and $\varepsilon_{th} = 0.0319$ [38]. A fiber volumetric fraction $V_f = 0.6$ has been applied for the reinforcement.

Evaluation of the surface crack propagation and fatigue life

Based on the SIF calculation at the deepest point and the surface point by the analytical approach, the Paris law is utilized [20] to determine the crack growth rate. This law

allows for the calculation of incremental changes in crack length and depth with each cyclic loading, thereby capturing the crack propagation process over time. For automated analysis, an in-house Python program has been developed, which employs an algorithm outlined in the flow chart depicted in Fig. 19.7. This program not only calculates the crack growth process but also provides visualizations of the real-time interfacial bond condition between the FRP and metal, as well as the interfacial fatigue damage. The same bending moment is applied on the pipes in the analytical approach which is identical to the fatigue test with the maximum applied load, with a stress ratio $R = 0.1$ to calculate the fatigue crack propagation rate. The same methodology of using the Paris' law as the FEA has been adopted to calculate the relation between crack size and the cyclic numbers, as well as the Paris' constants.

19.5 Results and discussion

In this subsection, we present and compare results across the experimental, FEA, and the analytical approaches. In addition, FEA and analytical results have been validated by the experimental results. Stress reduction, crack propagation, and the interfacial bond condition have been discussed successively.

19.5.1 Stress reduction owing to FRP repairing

The von Mizes stress distributed globally throughout the pipe model and locally around the surface crack is shown in Fig. 19.8. The stress distribution results indicate the composite reinforcement with four layers of CFRP laminates has significantly decreased the stress concentration, the maximum stress value drops from 472.6 to 374.6 MPa, by 20.7%. Moreover, the position that has the maximum stress value has shifted from the surface point to the deepest point along the crack front because of the composite reinforcement. The stress value at the surface point drops from 472.6 to 353.4 MPa, by 25.2%, while the stress value at the deepest point only drops 9.0%, from 411.3 to 374.4 MPa. This phenomenon is an evidence that the composite reinforcement performs better on decreasing the crack growth along the length direction than along the depth direction.

19.5.2 Experimental validation on the FEA and the analytical approach on the crack propagation

Surface crack propagations of three scenarios, i.e., PE-1-R, PE-1-R8, and PE-1-R45 are calculated by the FEA in Section 19.3 and the analytical approach in Section 19.4, added by an FEA an ANA suffix, respectively. Whereas the name with suffix represents the experimental results, i.e., PE-1-R(1). Their comparison with the experimental results are illustrated in Figs. 19.9–19.11. The results clearly demonstrate that the FEA and the analytical approach, which considered the crack-bridging effect (PE-1-R ANA), could accurately predict the surface crack growth in pipes reinforced with FRP subjected to cyclic bending.

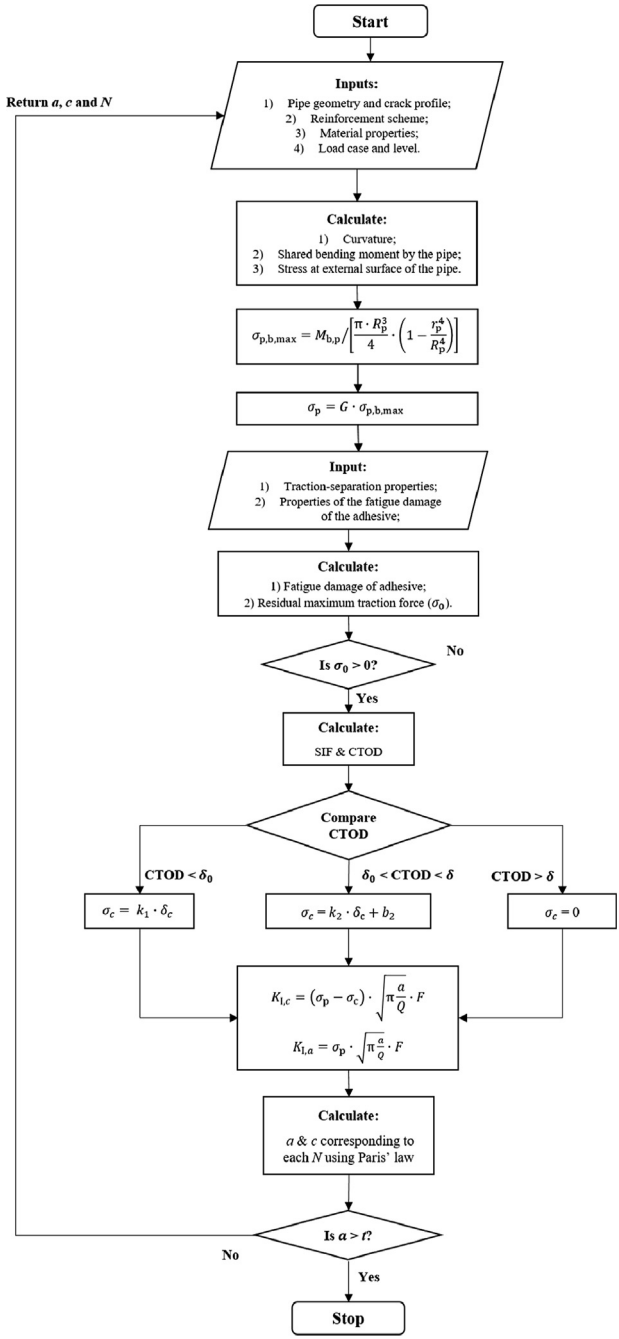

19.7 Algorithm of the analytical approach.

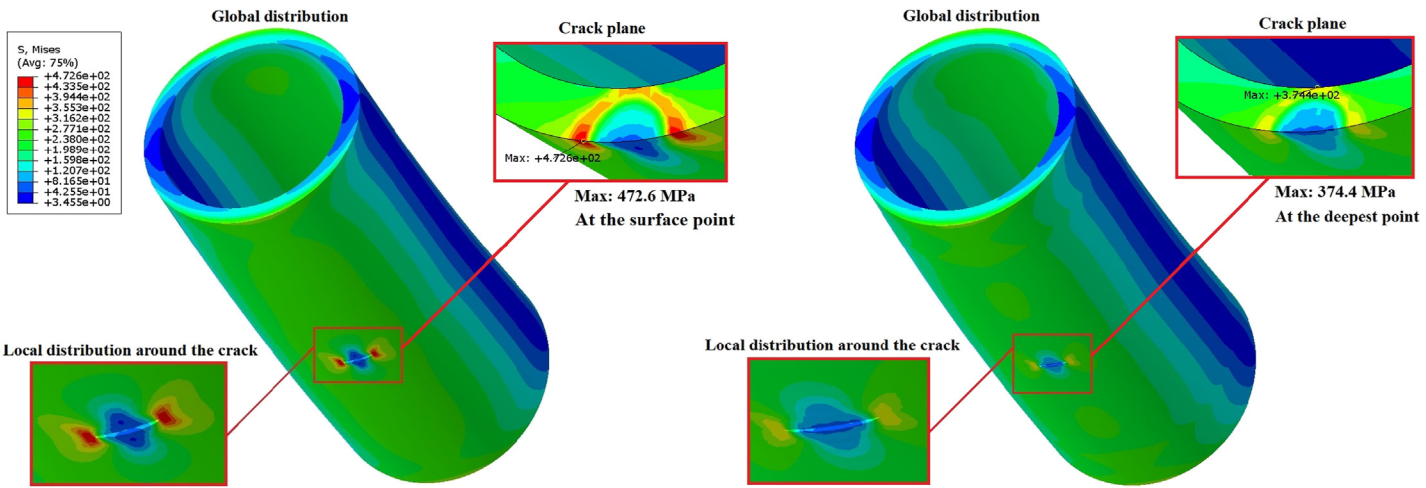

19.8 Global and local von Mizes stress distribution of the pipe model with large surface crack ($a = 10.64$ mm and $c = 12.15$ mm).

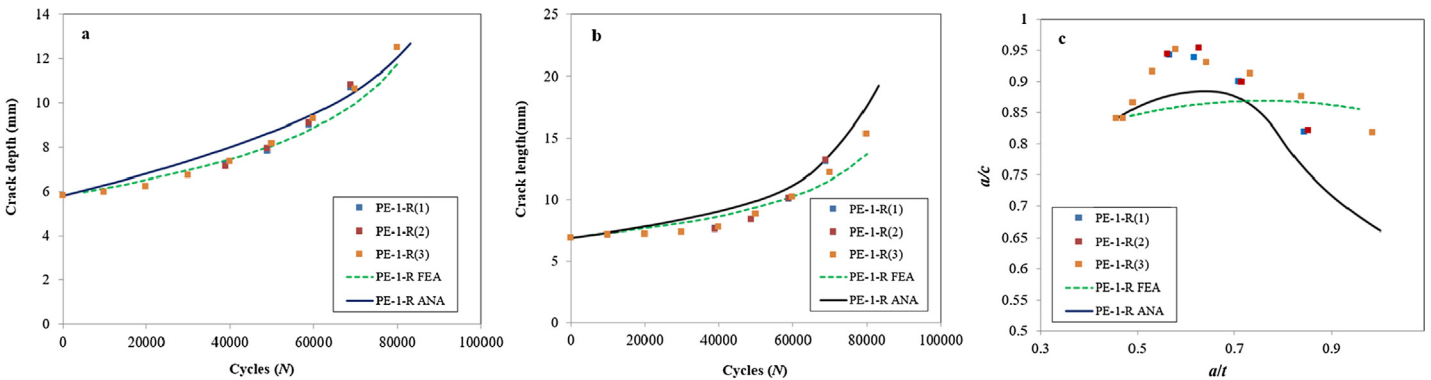

19.9 The comparison of FEA results and the analytical results with experimental results for external surface crack growth using four layers CFRP: (a) crack growth along the depth direction; (b) crack growth along the length direction; (c) aspect ratio variation with the crack growth.

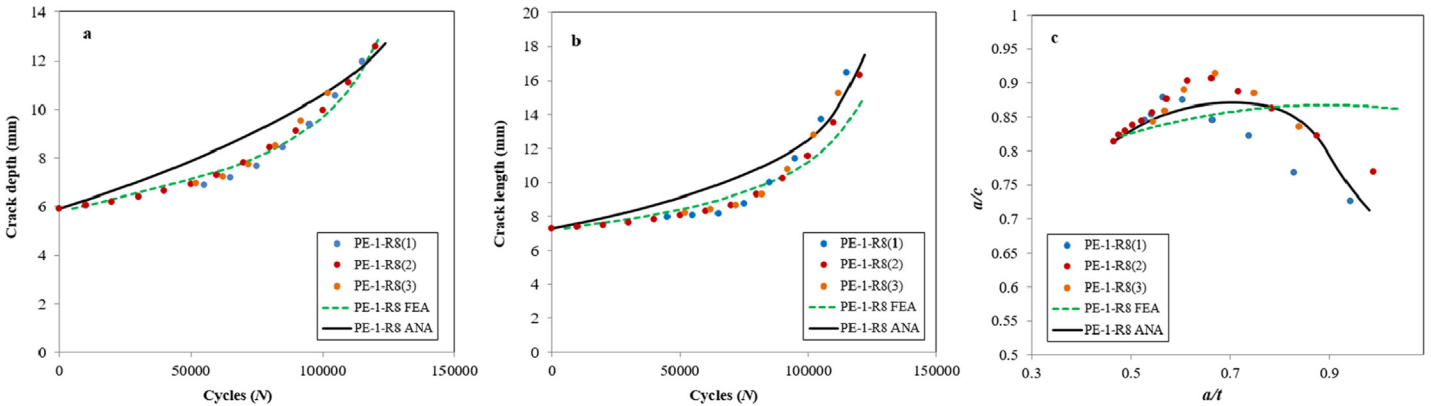

19.10 The comparison of FEA results and the analytical results with experimental results for external surface crack growth of using eight layers of CFRP: (a) crack growth along the depth direction; (b) crack growth along the length direction; (c) aspect ratio variation with the crack growth.

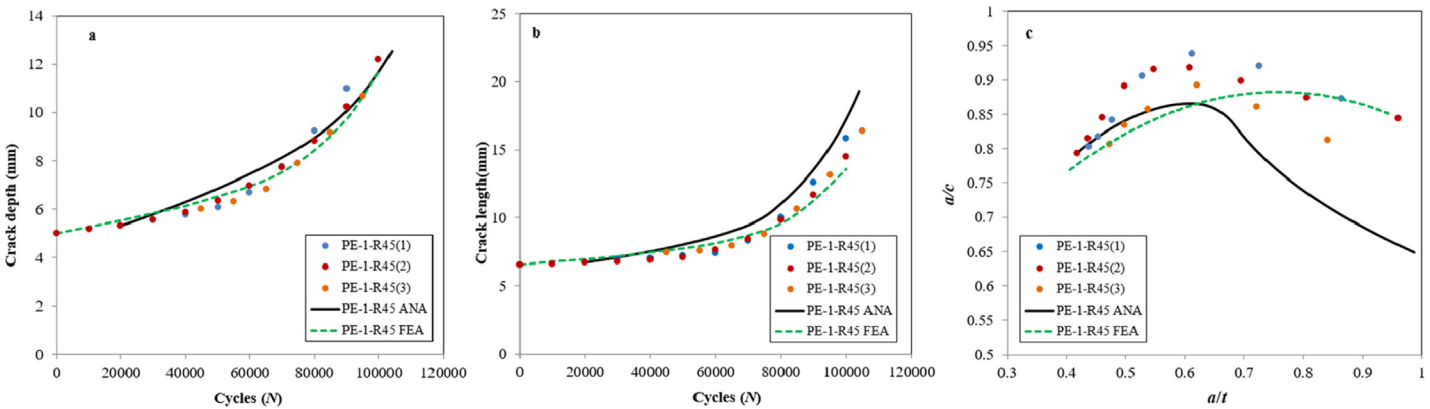

19.11 The comparison of FEA results and the analytical results with experimental results for external surface crack growth of using the inversely diagnose wrapping pattern: (a) crack growth along the depth direction; (b) crack growth along the length direction; (c) aspect ratio variation with the crack growth.

The FE model combined with the Paris' law can accurately predict the residual fatigue life of surface cracked steel pipes reinforced with composite. In addition, the results indicate that FRP reinforcement has significantly decreased the surface crack growth and prolonged the residual fatigue life of cracked models. For instance, without reinforcement, the PE-1(3) specimen only has a residual fatigue life of around 30,000 cycles start from the crack depth $a = 6.02$ mm to the crack depth $a = 10.8$ mm. While using eight layers of CFRP laminates to reinforce the surface cracked pipe at the same statue ($a = 6.02$ mm) has prolonged the residual fatigue life for around 4.5 times.

The predicted residual fatigue lives using the analytical approach of PE-1-R, PE-1-R8, and PE-1-R45 have 2.75%, 1.67%, and 3.75% differences with respect to the experimental results. In addition, the analytical approach is able to capture the sharp increasing of crack propagation rate along the length direction owing to the FRP-to-steel bond failure, which also reproduces the turning point of the variation of the aspect ratios (a/c).

The results shown the FEA performed better than the analytical approach over the crack depth prediction, maybe owes to the mixed-mode traction-separation model. However, the analytical approach worked better than the FEA over the crack length evolvement because of its consideration on the fatigue damage within the FRP-to-steel interface. This consideration contributed to a better prediction over the variation of the aspect ratio as well, indicated by Figs. 19.9c–19.11c.

19.5.3 Interfacial bonding condition

The interfacial bond condition along with the surface crack growth is analyzed. Crack sizes were extracted from the experimental specimen of PE-1-R(3) from the beginning of the crack growth to a larger crack size before penetrating the pipe wall. Each adjacent crack size has an interval of 10,000 cycles. The FE model in this part is in accordance with the FE models reinforced with four layers of CFRP. The interfacial bond conditions of models with different crack sizes, represented by the SDEG value, are shown in Fig. 19.12. It was only until the crack grew to a relatively large size ($a = 9.3$ mm, $c = 10.2$ mm) did the interfacial stiffness began to decrease, showing the maximum SDEG value reached 0.346. Then the maximum SDEG value slightly grew to 0.36 when the crack grew to the largest size, and the area of stiffness degradation expanded with a relatively low value.

The analytical approach was able to predict the maximum traction stress (σ_0) marked with solid lines, and the real-time traction stress (σ_c) applied on the crack surface, marked with dash lines (named as "TS", a.k.a. traction stress, e.g., PE-1-R TS), with respect to the nominal crack length, as shown in Fig. 19.13. The results demonstrate that the traction stress on PE-1-R8 which is reinforced with eight layers of CFRP, has the best performance in terms of the durability of the traction effectiveness. PE-1-R8 reached its maximum traction stress of 42.59 MPa when half the crack length ($c = 10.51$ mm) is 59.0% of final half the crack length ($c = 18.18$ mm) at failure, and the adhesive failed due to fatigue damage when the half crack length ($c = 14.53$ mm) reached 79.94% of the final half crack length. Due to the lowest efficiency of FRP reinforcement, PE-1-R45 quickly reaches its peak of traction stress of

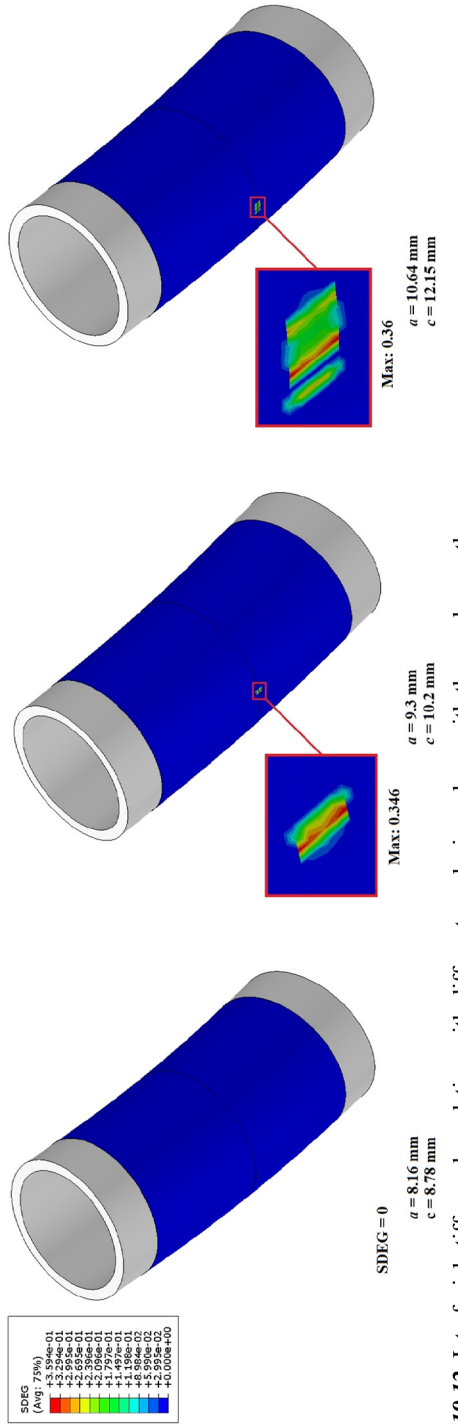

19.12 Interfacial stiffness degradation with different crack sizes along with the crack growth process.

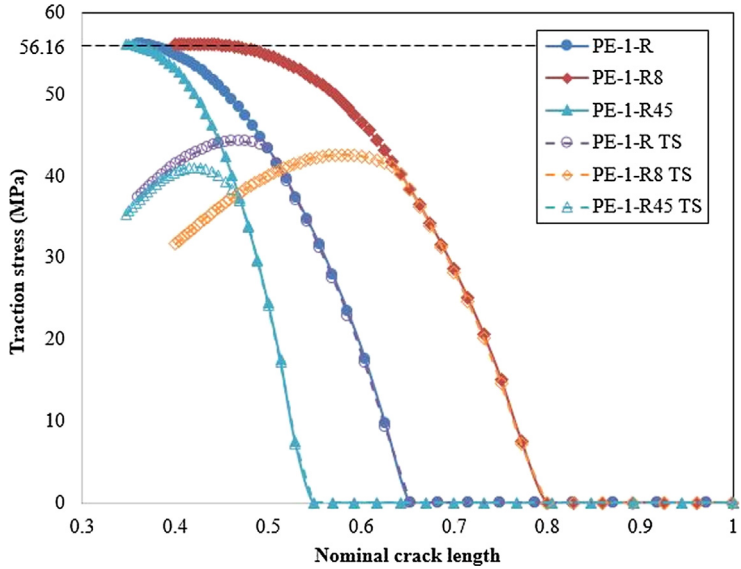

19.13 Peeling stress on the three FRP reinforced models, predicted by the analytical approach.

41.06 MPa at half the crack length of $c = 8.13$ (42.06% of the final half crack length), while quickly losing the traction at half the crack length of $c = 10.60$ mm (54.87% of final half the crack length). Therefore, we could infer that more efficient reinforcement schemes (e.g., applying more layers of CFRP, or using FRP with higher elastic modulus) would promote the effectiveness of the traction on the crack surface, which in return, would improve the overall reinforcement performance.

Furthermore, the ability of predicting surface crack growth in pipes with different dimensions (diameters and wall thicknesses) reinforced with FRP are investigated. Four different external diameters ranging from 168.3 to 323.8 mm with five different wall thicknesses from 10.97 to 21.95 mm are studied: five incremental pipe wall thickness has been discussed with $D = 168.3$ mm, while four incremental external diameter has been analyzed with $t = 12.7$ mm. These dimensions are chosen owing to their frequently usage in the offshore piping industry. The applied longitudinal stress statue generated by the bending moment of all models is identical to the FEA, remaining at 268.8 MPa (60% of the yield strength).

19.5.4 FEA validation on the analytical approach

The reduction in SIFs, which refers to the decrease in SIFs compared to the case of unreinforced surface cracks, is determined in this study. A crack size of $a = 5.98$ mm and $c = 7.12$ mm is employed for the analysis. The SIF reduction at the surface point (K_{IB}) resulting from the introduction of FRP reinforcement using the same wrapping scheme as the PE-1-R model is calculated and compared with the available FEA results [33], as summarized in Table 19.7. The obtained results

Table 19.7 Configurations of steel pipe models with different dimensions, and the results of the SIF decrease

Model No.	D (mm)	t (mm)	K_{IB} reduction (ANA) (%)	K_{IB} reduction (FEA) (%)	Difference between ANA and FEA (%)
1	168.3	10.97	30.1	29.5	2.0
2	168.3	12.70	27.7	27.3	1.5
3	168.3	14.27	26.1	26.0	0.4
4	168.3	18.26	23.6	23.8	0.8
5	168.3	21.95	22.2	22.6	1.8
6	219.1	12.70	26.9	28.2	4.6
7	273.0	12.70	26.4	25.3	4.3
8	323.8	12.70	26.0	24.6	5.7

demonstrate a close agreement between the analytical predictions and the FEA predictions, with minor differences ranging from 0.4% to 5.7%. This validates the capability of the analytical approach to accurately predict SIFs in FRP-reinforced surface cracked pipes of various dimensions. The analytical approach serves as a reliable tool for assessing the effectiveness of FRP reinforcement in reducing SIFs in surface cracked pipes.

19.6 Conclusion

Upon the comprehensive investigation and analysis through experimental, FEA, and analytical approaches, the following conclusions can be drawn based on the results from the three approaches:

- FRP performed more efficiently on reducing the fatigue crack growth rate along the length direction than along the depth direction, resulting in the increase of the preferred aspect ratio, owing to the crack-bridging effect.
- The FEM is able to accurately evaluate the SIF of the external surface crack in the FRP repaired metallic pipes subjected to cyclic bending, by considering the crack-bridging effect and the interfacial bond condition.
- The analytical approach managed to take critical factors including crack-bridging effect, stiffness degradation, and fatigue failure of the FRP-to-metal interface simultaneously.
- The analytical approach demonstrates exceptional accuracy in forecasting surface crack growth, accommodating various pipe dimensions and wrapping schemes. It allows for a quantitative assessment of influential parameters pertaining to material properties, interfacial characteristics, and reinforcement strategies, providing valuable insights for designing FRP reinforcement in surface-cracked pipes.

This research incorporates into pipe repairing standards such as ASME PCC-2 [47] and BS EN ISO 24817:2015 [48], as it offers a robust framework for guiding effective FRP reinforcement design and implementation, as well as offering an accurate

evaluation on the postrepair residual fatigue life. Detailed information for the experimental approaches can be reached at Ref. [16,34]. In addition to the external surface cracks, surface cracks on the internal surface has been investigated through FEA [19] and the analytical approach [49] as well. In addition, parametric studies has been conducted for the quantitative analysis of the reinforcement schemes and on a wide range of pipe dimensions [19,33]. All these studies present a relatively complete study on using the FRP to repair surface cracked metallic pipes [50].

References

[1] Saeed N, Ronagh H, Virk A. Composite repair of pipelines, considering the effect of live pressure-analytical and numerical models with respect to ISO/TS 24817 and ASME PCC-2. Composites Part B: Engineering 2014;58:605−10.

[2] Ghaffari MA, Hosseini-Toudeshky H. Fatigue crack propagation analysis of repaired pipes with composite patch under cyclic pressure. Journal of Pressure Vessel Technology, Transactions of the ASME 2013;135(3). https://doi.org/10.1115/1.4023568.

[3] Brahim AO, Belaidi I, Khatir S, Le Thanh C, Mirjalili S, Wahab MA. Strength prediction of a steel pipe having a hemi-ellipsoidal corrosion defect repaired by GFRP composite patch using artificial neural network. Composite Structures 2023;304:116299.

[4] Alsharif ZA. Design model of damaged steel pipes for oil and gas industry using composite materials. Part II: modeling. Advanced Structured Materials 2014;54:147−56. https://doi.org/10.1007/978-3-319-07383-5_12.

[5] Skarakis I, Chatzopoulou G, Karamanos SA, Tsouvalis NG, Pournara AE. CFRP reinforcement and repair of steel pipe elbows subjected to severe cyclic loading. Journal of Pressure Vessel Technology, Transactions of the ASME 2017;139(5):051403. https://doi.org/10.1115/1.4037198.

[6] Reis J, Costa A, da Costa Mattos H. Repair of damage in pipes using bonded GFRP patches. Composite Structures 2022;296:115875.

[7] Saffar A, Darvizeh A, Ansari R, Kazemi A, Alitavoli M. Prediction of failure pressure in pipelines with localized defects repaired by composite patches. Journal of Failure Analysis and Prevention 2019;19(6):1801−14. https://doi.org/10.1007/s11668-019-00781-0.

[8] Abd-Elhady AA, Sallam HEDM, Alarifi IM, Malik RA, El-Bagory TMAA. Investigation of fatigue crack propagation in steel pipeline repaired by glass fiber reinforced polymer. Composite Structures 2020;242:112189. https://doi.org/10.1016/j.compstruct.2020.112189.

[9] Benyahia F, Albedah A, Bouiadjra BB. Stress intensity factor for repaired circumferential cracks in pipe with bonded composite wrap. Journal of Pressure Vessel Technology, Transactions of the ASME 2014;136(4):041201. https://doi.org/10.1115/1.4026022.

[10] Kong D, Zhou P, Li C, Hong B, Xian G. Stress intensity factor of through-wall-cracked steel pipe wrapped with prestressed CFRP composites. Engineering Fracture Mechanics 2023;283:109218. https://doi.org/10.1016/j.engfracmech.2023.109218.

[11] Linden JM, Köpple M, Elder D, Gibson AG. Fracture mechanics of crack propagation in composite repairs of steel pressure piping. Journal of Reinforced Plastics and Composites 2014;33(6):526−32. https://doi.org/10.1177/0731684413500366.

[12] Valadi Z, Bayesteh H, Mohammadi S. XFEM fracture analysis of cracked pipeline with and without FRP composite repairs. Mechanics of Advanced Materials and Structures 2020;27(22):1888−99. https://doi.org/10.1080/15376494.2018.1529844.

[13] Zarrinzadeh H, Kabir MZ, Deylami A. Extended finite element fracture analysis of a cracked isotropic shell repaired by composite patch. Fatigue and Fracture of Engineering Materials and Structures 2016;39(11):1352−65. https://doi.org/10.1111/ffe.12446.
[14] Belhamiani M, Belhadri DE, Oudad W, Mansouri O, Bouzitouna WN. J integral computation and limit load analysis of bonded composite repair in cracked pipes under pressure. Frattura ed Integrità Strutturale 2019;13(50):623−37. https://doi.org/10.3221/IGF-ESIS.50.53.
[15] Wang L, Song S, Deng H, Zhong K. Finite-element analysis of crack arrest properties of fiber reinforced composites application in semi-elliptical cracked pipelines. Applied Composite Materials 2018;25(2):321−34. https://doi.org/10.1007/s10443-017-9621-9.
[16] Li Z, Jiang X, Hopman H, Zhu L, Liu Z. An investigation on the circumferential surface crack growth in steel pipes subjected to fatigue bending. Theoretical and Applied Fracture Mechanics 2019;105:102403.
[17] Branco R, Antunes FV, Costa JD. A review on 3D-FE adaptive remeshing techniques for crack growth modelling. Engineering Fracture Mechanics 2015;141:170−95. https://doi.org/10.1016/j.engfracmech.2015.05.023.
[18] Ghaffari MA, Hosseini-Toudeshky H. Fatigue crack propagation analysis of repaired pipes with composite patch under cyclic pressure. Journal of Pressure Vessel Technology 2013;135(3):031402.
[19] Li Z, Jiang X, Hopman H. Numerical analysis on the SIF of internal surface cracks in steel pipes reinforced with CRS subjected to bending. Ships and Offshore Structures 2019:1. https://doi.org/10.1080/17445302.2019.1702769.
[20] Li Z, Jiang X, Hopman H, Zhu L, Liu Z. Numerical investigation on the surface crack growth in FRP-reinforced steel plates subjected to tension. Theoretical and Applied Fracture Mechanics 2020;108:102659.
[21] Zarrinzadeh H, Kabir M, Deylami A. Crack growth and debonding analysis of an aluminum pipe repaired by composite patch under fatigue loading. Thin-Walled Structures 2017;112:140−8.
[22] Zheng B, Dawood M. Fatigue crack growth analysis of steel elements reinforced with shape memory alloy (SMA)/fiber reinforced polymer (FRP) composite patches. Composite Structures 2017;164:158−69.
[23] Belytschko T, Black T. Elastic crack growth in finite elements with minimal remeshing. International Journal for Numerical Methods in Engineering 1999;45(5):601−20.
[24] Fish J. The s-version of the finite element method. Computers & Structures 1992;43(3):539−47.
[25] Nguyen TN, Thai CH, Luu A-T, Nguyen-Xuan H, Lee J. NURBS-based postbuckling analysis of functionally graded carbon nanotube-reinforced composite shells. Computer Methods in Applied Mechanics and Engineering 2019;347:983−1003.
[26] Nguyen-Xuan H, Liu G, Bordas S, Natarajan S, Rabczuk T. An adaptive singular ES-FEM for mechanics problems with singular field of arbitrary order. Computer Methods in Applied Mechanics and Engineering 2013;253:252−73.
[27] Bocciarelli M, Colombi P, D'Antino T, Fava G. Intermediate crack induced debonding in steel beams reinforced with CFRP plates under fatigue loading. Engineering Structures 2018;171:883−93.
[28] Zheng B, Dawood M. Debonding of carbon fiber−reinforced polymer patches from cracked steel elements under fatigue loading. Journal of Composites for Construction 2016;20(6):04016038.
[29] Wang CH, Rose LRF. A crack bridging model for bonded plates subjected to tension and bending. International Journal of Solids and Structures 1999;36(13):1985−2014. https://doi.org/10.1016/S0020-7683(98)00070-5.

[30] Liu H, Xiao Z, Zhao XL, Al-Mahaidi R. Prediction of fatigue life for CFRP-strengthened steel plates. Thin-Walled Structures 2009;47(10):1069–77. https://doi.org/10.1016/j.tws.2008.10.011.
[31] Yu Q, Zhao X, Xiao Z, Chen T, Gu X. Evaluation of stress intensity factor for CFRP bonded steel plates. Advances in Structural Engineering 2014;17(12):1729–46.
[32] Wang H, Wu G, Pang Y. Theoretical and numerical study on stress intensity factors for FRP-strengthened steel plates with double-edged cracks. Sensors 2018;18(7):2356.
[33] Li Z, Jiang X, Hopman H. External surface cracked offshore pipes reinforced with composite repair system: a numerical analysis. Theoretical and Applied Fracture Mechanics 2022;117:103191.
[34] Li Z, Jiang X, Hopman H, Zhu L, Liu Z. External surface cracked offshore steel pipes reinforced with composite repair system subjected to cyclic bending: an experimental investigation. Theoretical and Applied Fracture Mechanics 2020;109:102703.
[35] Barenblatt G. Equilibrium cracks formed on a brittle fracture. Doklady Akademii Nauk SSSR 1959;127(1):47–50.
[36] Dugdale DS. Yielding of steel sheets containing slits. Journal of the Mechanics and Physics of Solids 1960;8(2):100–4.
[37] Barenblatt GI. The mathematical theory of equilibrium cracks in brittle fracture. Advances in Applied Mechanics 1962;7:55–129.
[38] Khoramishad H, Crocombe A, Katnam K, Ashcroft I. Predicting fatigue damage in adhesively bonded joints using a cohesive zone model. International Journal of Fatigue 2010;32(7):1146–58.
[39] API SPEC 5L: specification for line pipe. Washington, DC: API; 2018.
[40] Faserverbundwerkstoffe. Technical data: Epoxy resin L 20. https://www.swiss-composite.ch/pdf/t-Epoxydharz-L20-e.pdf
[41] ASTM, ASTM E2899. Standard test method for measurement of initiation toughness in surface cracks under tension and bending. West Conshohocken, United States: ASTM; 2019.
[42] ASTM, ASTM E647. Standard test method for measurement of fatigue crack growth rates. 1994.
[43] Kim S, Kim M-H. Dynamic behaviors of conventional SCR and lazy-wave SCR for FPSOs in deepwater. Ocean Engineering 2015;106:396–414.
[44] Xia S, Teng J. Behaviour of FRP-to-steel bonded joints. In: Presented at the proceedings of the international symposium on bond behaviour of FRP in structures, Hong Kong, 7–9 December 2005; 2005. p. 419–26.
[45] Abaqus. "Test configurations for Abaqus 2021 products." Dessault System. https://www.3ds.com/support/hardware-and-software/simulia-system-information/abaqus-2021/
[46] Anderson TL. Fracture mechanics: fundamentals and applications. CRC Press; 2017.
[47] ASME. ASME PCC-2: repair of pressure equipment and piping. American Society of Mechanical Engineers; 2015.
[48] BS, BS EN ISO 24817:2015. Petroleum, petrochemical and natural gas industries-composite repairs for pipework-qualification and design, installation, testing and inspection. British Standards Institution; 2015.
[49] Li Z, Jiang X, Hopman H, Affolter C. Surface crack growth in metallic pipes reinforced with Fibre-Reinforced Polymers subjected to cyclic loads: an analytical approach. Theoretical and Applied Fracture Mechanics 2023;127:104070.
[50] Li Z. Surface crack growth in metallic pipes reinforced with composite repair system, T2021/8 ed. (no. 8). Delft: TRAIL Research School; 2021.